

Mesoscale Surface Patterning of a Laterally-Grafted Rod Amphiphile: Rings And Fibers

Libin Liu,^[a, b] Jung-Keun Kim,^[a] and Myongsoo Lee^{*[a]}

An aromatic amphiphilic molecule based on branched oligo(ethylene oxide) was synthesized. Evaporation-driven ring formation and Langmuir–Blodgett films are investigated by utilizing this rigid–flexible block molecule. The size of the rings is strongly dependent on the solvent evaporation rate and the concentration of the molecule. In case of fast evaporation, volcano-like rings are formed by evaporating solution of high concentration. Perfectly symmetrical rings with diameters in the range of 2–6 μm are obtained by evaporating solution of low concentration. The formation mechanism of the ring is briefly discussed. The molecule at the air–water interface ex-

hibits excellent amphiphilic properties. Upon transferring the monolayer onto solid substrates, AFM revealed the formation of fine and long, straight fibers. By combining the data obtained from the isotherms, AFM, water contact angle measurements, and UV/Vis and fluorescence spectra, the fibers are suggested to be formed by π – π stacking interaction of the aromatic rod segments as the oligo(ethylene oxide) branches are submerged in the water subphase upon compression. The fiber formation is associated with the transformation of the aromatic rod segments from the face-on conformation to the edge-on conformation.

1. Introduction

Surface patterning for the fabrication of structures defined at the micrometer and/or nanometer length scales has received growing interest over the past few decades as a consequence of its potential applications in several scientific and technological fields, such as photonics,^[1] optoelectronics,^[2] microchip reactors,^[3] and miniaturized sensors.^[4] There are two main strategies in surface patterning. One is the top-down approach such as photolithography, e-beam lithography, soft lithography, dip-pen lithography, constructive nanolithography, and nanoimprinting lithography.^[5–9] The disadvantage of most top-down strategies is that they are very elaborate and are usually time-consuming. The other is the bottom-up approach that utilizes self-assembly and self-organization of molecules or simple basic building blocks in order to achieve regular structures.^[10] Most bottom-up strategies that use self-assembly are much simpler and can often cover arbitrary sized areas during the process. The self-assembly and self-organization processes and the properties (shape, size, function, etc.) of the patterns can be controlled by tailoring the properties of the building blocks.

Droplet evaporation is a simple patterning method and has recently been employed to create patterns via the dynamic self-assembly of nonvolatile dispersed solute particles.^[11] Okubo and co-workers reported the formation of dissipative structures in the course of drying a colloidal solution and conducted rheological and kinetic analyses.^[12] Shimomura et al. employed dissipative patterns formed by drying a polymer colloidal solution for mesoscopic patterning.^[13] Gelbart et al. have demonstrated the mechanism of solvent dewetting in submonolayer annular arrays formed by drying organically passivated metal colloids on a substrate.^[14] Brinker and co-workers developed evaporation-driven self-assemblies that enable the rapid production of patterned mesoporous and nanocomposite ma-

terials in the form of films, fibers, or powders.^[15] Sommer and colleagues obtained circular deposition patterns in evaporating drops of polymer aqueous suspensions.^[16] In general, when a droplet or a film of liquid is evaporated on a substrate, although a variety of patterns might form, the pattern formed most often after drying is a dense, ring-like deposit along the perimeter of the initial droplet. The distribution evolution of a solute during the droplet-drying process is a consequence of the interplay among many factors, including wetting properties, surface tension (Marangoni effect), capillary forces, gravity effect, and convective flow. The complex interplay of evaporation, film rupture instabilities, and hydrodynamics defines a rich class of systems which might become available for molecular assembly governed by nonequilibrium processes rather than equilibrium processes. Therefore, the droplet-drying process may be developed as a potentially simple approach to direct the movement of the solutes and eventually pack them into a desired structure.

The opportunities for experimental control of the key physical influences on solute distribution (evaporation flow, gravitation, temperature gradient, and interaction with substrate and other solutes)^[17] in the evaporating drop experiment have not yet led to exploration of systems containing nanoscale rigid–

[a] L. Liu, J.-K. Kim, Prof. M. Lee
Center for Supramolecular Nano-Assembly
Department of Chemistry, Seoul National University
Seoul 151-742 (Korea)
Fax: (+82) (2) 393-6096
E-mail: myongslee@snu.ac.kr

[b] L. Liu
Department of Chemistry
Yonsei University, Seoul 120-749 (Korea)

flexible block molecule solute (Figure 1). The fabrication of hierarchical luminescence patterns involving aromatic rigid-flexible block macromolecules is important to progress in technol-

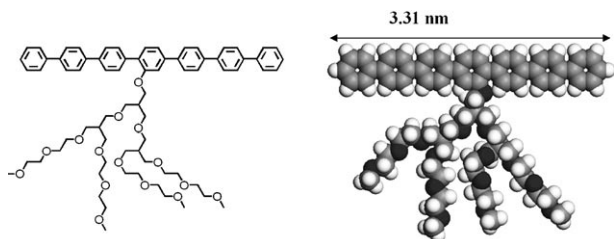


Figure 1. Chemical structure (left) and molecular model (right) of the rigid-flexible block molecule.

ogies such as drop-on-demand inkjet printing of small structures and arrays for organic displays, polymer-based electronics, combinatorial materials science.^[18]

Additionally, Langmuir-Blodgett technique is another efficient way toward the fabrication of laterally patterned structures on solid supports.^[19] Amphiphilic molecules with a polar head group and a long hydrophobic tail can form a stable monolayer at the air-water interface. Under compression the hydrophilic group can be incorporated into the water subphase and the hydrophobic group will keep away from the water subphase, thus changing the effective composition at the air-water interface. Upon deposition the morphologies of the molecules could be transferred to solid substrate, thus called Langmuir-Blodgett patterning.^[20]

Rigid-flexible block molecules as a novel type of block copolymer consisting of a rigid rod and a flexible coil, are excellent candidates for creating well-defined supramolecular structures via a process of spontaneous organization.^[21] The optical fluorescence property of the rigid-flexible block molecules and their tendency to stack and hence form supramolecular structures on the basis of the interaction of aromatic rod segments motivate us to study the surface patterning of evaporation-driven ring formation and Langmuir-Blodgett film involving a novel rigid-flexible block molecule.

Experimental Section

Synthesis of Rigid-Flexible Block Molecules: The synthesis of the laterally-grafted rod-coil molecule was performed with the preparation of an oligoether dendron according to a procedure described previously.^[22] The ter(*p*-phenylene) aromatic scaffold was prepared from etherification with 1,4-dibromo-2-hydroxybenzene and tosylated oligoether dendrons, and then subsequent Suzuki coupling reaction with a boronic acid derivative. The final rod-coil molecule was synthesized by the Suzuki coupling reaction with an aromatic scaffold and biphenyl units. ¹H and ¹³C NMR spectra were recorded from CDCl₃ solution on a Bruker AM 250 spectrometer. The purity of the products was checked by thin-layer chromatography (TLC; Merck, silica gel 60 F₂₅₄). Microanalyses were performed with a Perkin-Elmer 240 elemental analyzer at the Organic Chemistry Research Center. MALDI-TOF-MS was performed on a Perceptive Biosystems Voyager-DE STR using a 2,5-dihydroxybenzoic acid matrix.

Recycling preparative high-performance liquid chromatography (HPLC) was performed at room temperature using a 20 mm × 600 mm polystyrene column on a Japan Analytical Industry Model LC-908 recycling preparative HPLC system, equipped with UV detector 310 and RI detector RI-5. Yield: 62%. ¹H NMR (250 MHz, CDCl₃, ppm): δ = 7.71–7.33 (m, 28H; Ar-H), 7.23 (s, 1H; Ar-H; *o* to -CH₂OAr), 4.18 (s, 2H; -CH₂OAr), 3.57–3.36 (m, 60H; -CH₂O), 2.12–2.05 [m, 3H; -CH(OCH₂)₂]; ¹³C NMR (65 MHz, CDCl₃): δ = 156.32, 141.21, 140.58, 140.14, 139.77, 139.65, 139.38, 138.86, 137.27, 130.99, 130.03, 129.32, 128.79, 127.51, 127.36, 119.53, 111.01, 72.01, 70.60, 69.92, 69.65, 66.62, 59.30, 40.16, 39.91 ppm. MALDI-TOF-MS: *m/z* ([*M*+Na]⁺) 1245.53, Found 1247.35. Anal. Calcd. for C₇₄H₉₄O₁₅: C, 72.64; H, 7.74. Found: C, 72.57; H, 7.68.

Droplet Experiments: A 40–50 μL droplet of the molecule at a concentration of 0.05 and 0.2 mg mL⁻¹ in chloroform (HPLC grade) was deposited on a 1 × 1 cm² silicon wafer in air and in a sealed bottle, respectively. Dynamic light scattering experiments revealed no aggregates forming at the experimental concentration. The droplet remained on its support until the solvent was totally evaporated (solvent cannot escape from the silicon wafer). For the droplet in air, it took half an hour to evaporate completely, whereas in the sealed bottle, the evaporation was generally completed overnight. Highly polished [100] silicon wafers (Semiconductor Processing Co.) were cut into rectangular pieces and sonicated in Nanopure water (18.2 MΩ cm) for 10 min to remove silicon dust. The wafers were then chemically treated with piranha solution (30% concentrated hydrogen peroxide, 70% concentrated sulfuric acid, **Caution: hazardous solution!**) for 1 h to strip off any organic contaminants that cling to the silicon oxide surface, while at the same time oxidizing/hydroxylating the surface.^[23] Subsequent rinsing with Nanopure water resulted in a fresh silicon oxide layer with a high concentration of silanol groups. Finally, the wafers were abundantly rinsed with Nanopure water and dried at room temperature. For fluorescence microscopy experiments, the droplet was deposited on cover glass.

Langmuir-Blodgett (LB) Films: Langmuir isotherms at the air-water interface and LB depositions onto a silicon substrate were conducted at room temperature using a KSV minitrough system (KSV Instruments Ltd.) equipped with two moving barriers and a Wilhelmy plate for measuring surface pressure according to the usual procedure.^[24] Between runs, the trough was cleaned with acetone and rinsed several times with Nanopure water. A dilute solution (40–120 μL, 0.05–0.2 mg mL⁻¹) in chloroform was deposited in 5–10 drops uniformly distributed on the Nanopure water surface and left to evaporate and spread evenly for 30 min. The spreading solvent concentrations show no effect on the surface behavior of the molecule. The compression rate was kept at 5 mm min⁻¹ until the desired surface pressure was reached. For AFM measurements, the monolayer LB films of the rigid-flexible block molecule were transferred at a rate of 2 mm min⁻¹ onto silicon wafers at various surface pressures by the upstroke mode of the vertical dipping method. For UV/Vis and fluorescence spectral measurements, the floating films were transferred onto quartz at selected surface pressures by the horizontal Langmuir-Schaefer method and with a certain number of depositions. The typical transfer ratio was in the range of 0.8 to 0.9, which suggests a good film quality.

Characterization: Atomic force microscopy (AFM) was performed in the tapping mode under ambient conditions with a Veeco NanoScope IIIa atomic force microscope (Digital Instruments, Inc., Santa Barbara, CA) using Nanosensors silicon probes (dimensions: *H* = 3.5–4.5 μm, *W* = 30–40 μm, *L* = 115–135 μm). An amplitude ratio of 0.95 and higher was employed to avoid monolayer damage.^[25] The

AFM scans were conducted at a scanning rate of 0.5–2 Hz. All images were processed with a second-order flattening routine. The field-emission scanning electron microscopy (FE-SEM) was recorded on a JEOL NSM-6500F microscope at an acceleration voltage of 12 kV. The water contact angle was measured by optical microscope equipped with a CCD camera at ambient conditions at a relative humidity of 52%. UV/Vis and fluorescence spectra measurements of the films were performed at room temperature using UV-1650PC spectrophotometer and a Hitachi F-4500 fluorescence spectrometer, respectively. The fluorescence microscopic images were obtained with Nikon Eclipse TE2000-U, inverted fluorescence microscope equipped with DXM1200C digital camera, using a high-pressure mercury lamp (100 W) as a light source and a UV-2 A filter.

2. Results and Discussion

2.1. Evaporation-Driven Ring Formation

The microscopy morphologies of the self-assembled structures depend on the starting concentration of the rigid-flexible block molecules prior to deposition. Figure 2 shows the ring structures resulting from the evaporation of 0.2 mg mL^{-1} CHCl_3

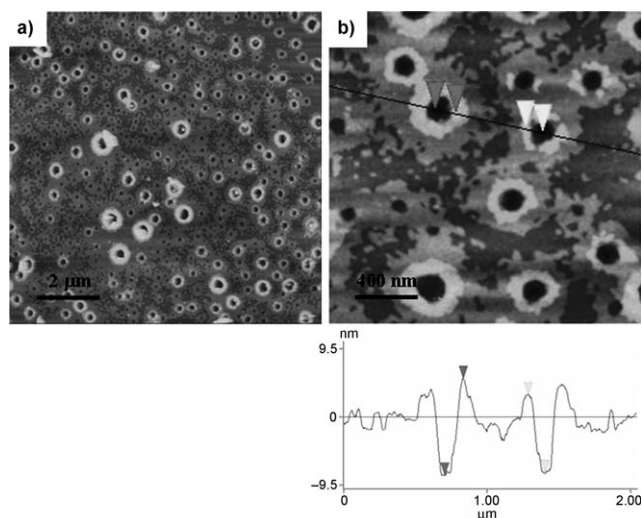


Figure 2. A 40–50 μL droplet at a concentration of 0.2 mg mL^{-1} deposited on silicon wafer in air. AFM images of a) a $10 \times 10 \mu\text{m}^2$ scan and b) a $2 \times 2 \mu\text{m}^2$ scan and its cross-sectional analysis.

droplets of rigid-flexible block molecules in air. High-magnification AFM images reveal these structures as volcano-shaped with microdomains in the surroundings of the ring. The size of the ring is 100–500 nm in diameter and 10–15 nm in height. The rim is in the range of 100 nm to 200 nm. The inside of the ring is almost empty as indicated by cross sectional analysis that reveals a peripheral profile lower than that of the ring.

The diameter of the ring can be tuned by varying the concentration. When a droplet of low concentration (0.05 mg mL^{-1}) of the rigid-flexible block molecules was deposited on the substrate, perfectly symmetrical rings are formed (Figure 3 a). The rim of the ring increases to about 300–500 nm with an average height of 20 nm. AFM scans performed in the

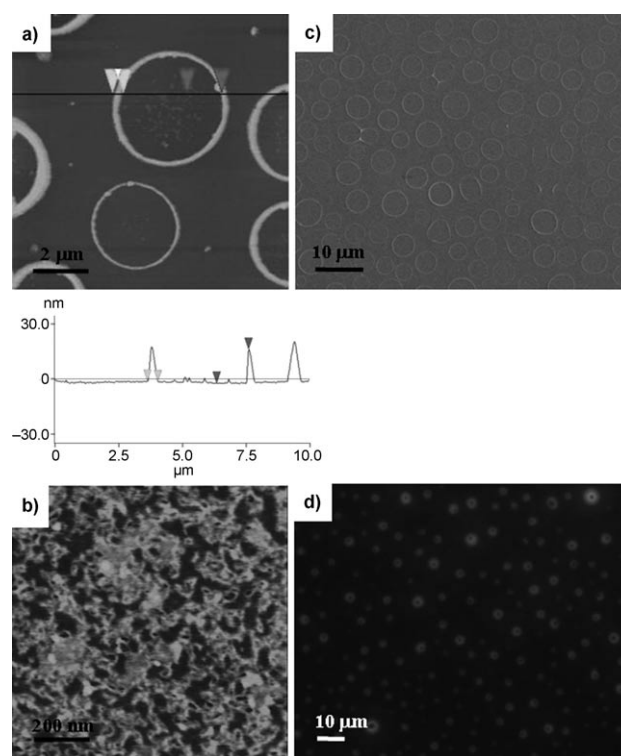


Figure 3. A 40–50 μL droplet at a concentration of 0.05 mg mL^{-1} deposited on a substrate in air. AFM images of a) a $10 \times 10 \mu\text{m}^2$ scan and its cross-sectional analysis and b) a $1 \times 1 \mu\text{m}^2$ scan; c) a low-magnification SEM image and d) a fluorescence microscopy image of the droplet deposited on a cover glass.

spacing area between the rings reveals the worm-like micelles deposited on the substrate (Figure 3 b). The width of the worm micelle is about 13 nm. It is composed of rigid-rod segments of the molecule in the core and the PEO branches surrounded in the shell, which may be formed by the aggregation of the molecules due to π - π stacking of the aromatic rod segments when the concentration of the droplet is higher than the critical micelle concentration during evaporation. A low-magnification SEM image shows the rings with a diameter of 2–6 μm uniformly distributed on the substrate (Figure 3 c). When the droplet is deposited on the cover glass, the rings are also visible by confocal laser scanning microscopy in the fluorescence mode (Figure 3 d). The observed diameters are in the same range as those observed by the electron microscopy and AFM. The fluorescence images of the film reveal that the ring structures have a fluorescence intensity higher than the periphery, produced by a continuous solute layer.

We ascribe the observed ring patterns to a transition from diffusive to convective fluid flow during evaporation as the starting molecular concentration decreases. At high molecular concentrations (e. g. 0.2 mg mL^{-1}), thermocapillary flow does not occur and volcano-like rings form as a result of hole nucleation and growth in the thin liquid film upon evaporation.^[14] In the absence of thermocapillary effects (i.e. convective motions in the fluid), the film thickness decreases homogeneously until reaching a critical thickness when the film becomes unstable and ruptures as observed microdomain in the AFM images

(Figure 2). The critical thickness depends on the disjoining pressure of the solvent film on the substrate. The hole opening pushes most molecules out along its advancing rim. In that case, isolated molecules and their aggregates can protrude from the solvent film and feel frictional forces due to attraction toward the solid substrates. When the frictional force is high enough to prevent the molecules from drifting, the pinning of the contact lines of nucleating holes occurs, resulting in a ring assembly. The interiors of the condensed rings are essentially free of adsorbed molecules. They have been swept to the perimeter during evaporation and incorporated in the growing ring. This was proved by the height profile which shows a high deepness of the inner compared with that of the surrounding of the ring.

At low concentrations (e.g. 0.05 mg mL^{-1}), a Marangoni instability dominates, giving rise to convective flow.^[26] The occurrence of the Marangoni instability depends on the temperature dependence of the surface tension, which was found to depend on the concentration of the molecule. Convective transport arises from temperature gradients due to evaporative cooling. The molecule in a concentrated solution can be more easily pinned compared with in a more dilute solution. On the contrary, the hole opening in a more dilute solution can evolve further, which results in a retarded pinning of the contact lines. Therefore, the average diameter of ring-like assemblies increases with decreasing concentration.

When the droplet evaporation was performed in a sealed bottle, the evaporation rate of the solvent was controlled. The decrease in the evaporation rate induces a decrease in the temperature gradient. The system equilibrates quicker than the heat loss by the evaporation process. The ring formation is inhibited by a slowdown of the hydrodynamics of the system, which causes a less efficient transport of the solute by the solvent. Under such conditions, shrinking of the film by mass loss occurs and the aggregates of the rigid-flexible block molecules, which occurs when the concentration is higher than the critical micelle concentration during solvent evaporation, uniformly distributed on the silicon wafer (Figure 4). The starting concentration of the droplet has no effect on the aggregates under such evaporation conditions. A higher concentration (0.2 mg mL^{-1}) of the droplet only reveals a denser distribution of the aggregates (images not shown). This means that forma-

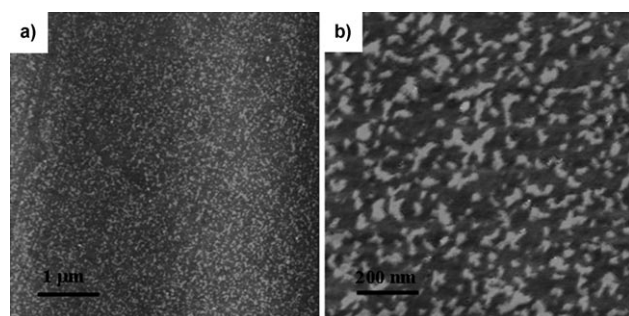


Figure 4. A 40–50 μL droplet at a concentration of 0.05 mg mL^{-1} deposited on silicon wafer in sealed bottle. AFM images of a) a $5 \times 5 \mu\text{m}^2$ scan and b) a $1 \times 1 \mu\text{m}^2$ scan.

tion of rings, induced by a fast evaporation process, is related to the instabilities.

2.2. Langmuir-Blodgett Films

The molecules with rigid, hydrophobic backbones and branched, flexible, hydrophilic PEO branches possess excellent amphiphilic properties. The surface-pressure–area (π – A) isotherm is shown in Figure 5a. When placed on water in dilute quantities, these molecules organize into dense monolayers

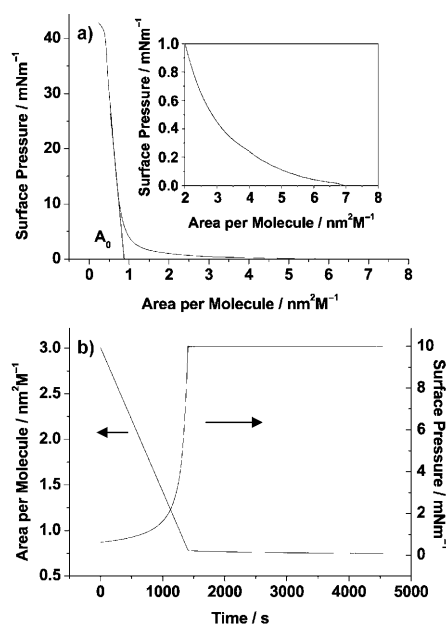


Figure 5. a) Surface-pressure–area isotherm of the rigid-flexible block molecule. Inset: High magnification of onset of the surface pressure. b) Changes in the surface area as a function of time and at a constant surface pressure of 10 mNm^{-1} .

with hydrophilic PEO chains adopting a pancake conformation adsorbing on the water surface, as demonstrated for a number of PEO-containing molecules.^[27,28] Considering the affinity of PEO for the air–water interface, we propose that the expanded region of the isotherm represents a film of PEO-tethered aromatic rod segments at the surface. The observed molecular area for the onset of the surface pressure is about 6.94 nm^2 (Figure 5a inset). This value is close to the surface area estimated for a molecule lying on the water surface with the aromatic rod segments adopting a face-on conformation and the PEO branches adsorbing on the water surface, which is about 7.03 nm^2 .^[29] Thus, we suggest that the onset of the surface pressure is caused by the initial interaction of hydrated PEO branches. Upon compression, it is expected that the PEO branches will be completely submerged in the water subphase at higher surface pressures and the steep rise in the surface pressure is mainly caused by crowding of the rigid-rod segments. This confirms the critical role of the hydrophobic rigid-rod segments in the surface behavior of the Langmuir monolayer at a high surface pressure. The films collapse at a surface

pressure of 42 mNm^{-1} . The limiting cross-sectional molecular area (A_0), calculated by extrapolating the steep rise in the surface pressure to zero, is 0.89 nm^2 . The theoretical surface area occupied by the hydrophobic rod block adopting an edge-on conformation is about 0.99 nm^2 as calculated by the Corey–Pauling–Koltun (CPK) model, similar to the limiting molecular area, indicating that compression leads to the change of the conformation of the aromatic rod segment. At this molecular area, the PEO branches are submerged into water and the area is only occupied by the aromatic rod segments standing on the water surface, which is consistent with AFM results.

Additionally, the stability of the spreading films on the water surface was also evaluated by measuring the π - t or A - t isotherms (Figure 5 b).^[30] The monolayer was compressed to a surface pressure of 10 mNm^{-1} and held constant at this value for a period of 70 min. The area per molecule decreased about 6 \AA^2 over the 70 min period. This value corresponds to $<7\%$ of the limiting molecular area of the monolayer. This slight decrease in the surface area is due to the rearrangement of the molecules to reduce the empty spaces in the monolayer or a partial aggregation of the molecules. Therefore, the film kinetic data suggest that a relatively stable monolayer is formed at the air–water interface.

When the monolayer was deposited on the silicon substrate, different morphologies were obtained (Figure 6). In all cases, AFM images show a full area coverage of the Langmuir–Blodgett monolayer film and high film transfer ratio (0.8–0.9). This indicates that the morphology of the formed monolayer at the

air–water interface is preserved upon transfer.^[31] At the onset of surface pressure (area/molecule of 6.9 nm^2), smooth and uniform films with a surface microroughness in the range of 0.2–0.3 nm were formed (calculated within $1 \times 1 \mu\text{m}$), as expected for low-molecular-weight rigid–flexible block molecules as well as for many flexible macromolecular materials.^[24b,32] Interestingly, when the surface pressure was increased to 1 mNm^{-1} , fine and long, straight fiber-like patterns appeared. The fibers are several micrometers in length and 80–90 nm in width. The height of the fiber is about 1.2 nm. This corresponds to the aromatic rod segments adopting vertical conformation topping the PEO branches beneath. When deposited onto a substrate, PEO branches adsorb onto the hydrophilic silicon wafer surface underneath the hydrophobic backbone, which translates into increased thickness. The distance between the fibers decreases as the surface pressure progresses, while the height of the fiber stays approximately constant. At a surface pressure of 10 mNm^{-1} , the fiber becomes more densely packed and the coverage is increased to 88%. Further compression leads to the connection of the fibers. In this state, the fibers cannot preserve their identity and merge into each other at the high density of molecular packing. Considering that the hydrophilic PEO branches would be immersed in the water by compression, the fibers should be formed by the packing of the aromatic rod segments due to the π - π stacking interaction, as shown in Figure 5 f. At a low surface pressure (in the liquid region) the parallel fibers cover a region of several micrometers and align along the deposition, which is because

the alignment of the transferred molecules parallel to the dipping direction is determined by the geometric conditions of the monolayer flow on the water subphase,^[33] indicating an important role of the lateral compression and vertical lifting in domain orientation as well as high mobility. At high surface pressure in the compact region the long-range ordered structures are more densely packed, but not correlated to the transfer direction (Figure 6 d), thus, they can not be induced by monolayer transfer.^[20d]

The surface composition of the deposited monolayer was also measured by the water contact angle. The deposited monolayers exhibit low to moderate hydrophobic character (contact angle in the range of 24 – 45°) indicating a mix surface composition (a contact angle of 80 – 120° is expected for surface composed of phenyl rings and below 10° for dry PEO surface). High

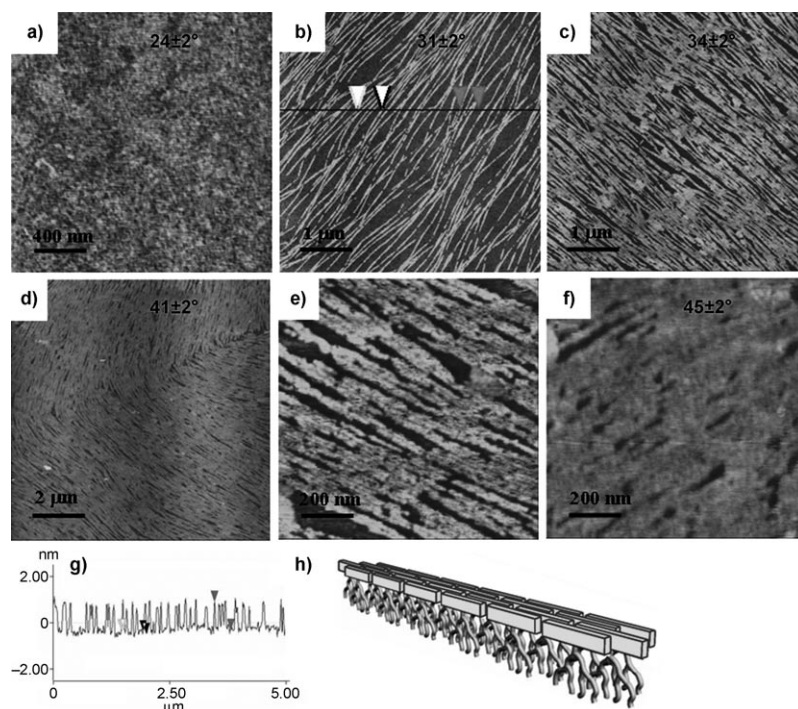


Figure 6. AFM images of Langmuir films deposited at different surface pressures. a) a $2 \times 2 \mu\text{m}^2$ scan at the onset of surface pressurization, b) a $5 \times 5 \mu\text{m}^2$ scan at 1 mNm^{-1} , c) a $5 \times 5 \mu\text{m}^2$ scan at 5 mNm^{-1} , d) a $10 \times 10 \mu\text{m}^2$ scan at 10 mNm^{-1} , e) a $1 \times 1 \mu\text{m}^2$ scan at 10 mNm^{-1} , f) a $1 \times 1 \mu\text{m}^2$ scan at 30 mNm^{-1} , g) Line cross-sectional analysis (line in b) and h) proposed molecular model of the fiber. The corresponding water contact angles are inserted in selected images.

surface pressure leads to a more densely packed fibers and a high water contact angle (Figure 5 insets). This suggests slight increase in hydrophobicity, which is associated with greater exposure of the benzene ring and some screening of the PEO branches.

To further confirm the structural change of the transferred film caused by π - π stacking interaction of the aromatic segments, UV/Vis and fluorescence spectra were obtained. Figure 7a shows the UV/Vis spectra of the molecule both in solution and in LB films. The UV/Vis spectrum of the molecule in

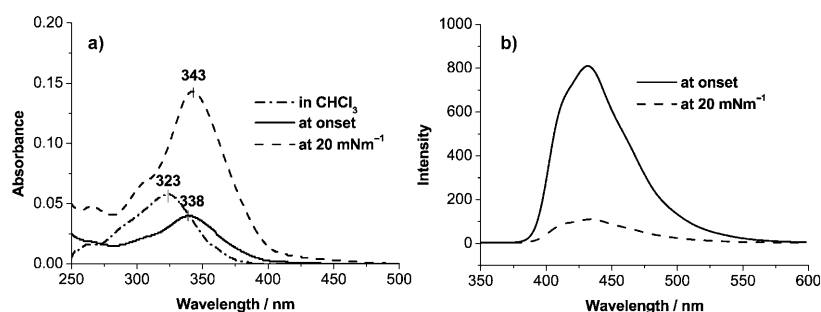


Figure 7. a) UV/Vis and b) fluorescence spectra of 20-layer LB films of the molecule deposited on quartz.

solution exhibits an absorption band at 323 nm, corresponding to monomer. The bands of the LB films deposited at both onset and high surface pressure of 20 mNm^{-1} locate at 338 nm and 343 nm, respectively, indicating a red-shift in comparison with that of the solution. The red-shift of the onset of the surface pressure should be ascribed to the planarization of the aromatic rod segments induced.^[34] In addition, the band at a high surface pressure of 20 mNm^{-1} is further red-shifted compared with that of the onset of the surface pressure, indicating that J-aggregate forms in the LB films when the molecules are co-facially arranged in the edge-on conformation within the fiber.^[35] This should be distinguished from the red-shift owing to planarization alone at the onset of the surface pressurization.^[34,36] The characteristic of a π -aggregated state of the film deposited at high surface coverage was also confirmed by fluorescence spectra (Figure 7b), where the intensity of the film deposited at 20 mNm^{-1} was distinctly quenched compared to that of the film deposited at the onset of surface pressurization.

The Langmuir–Blodgett technique provides a powerful method to control the molecular arrangement in the two-dimensional air–water interface. Continuous compression reduces the area available for the molecules and leads to complete dissolution of the flexible PEO chains into water and further to reorientation of the aromatic rod segments to a vertical position to accommodate the greatly reduced surface area. The ratio of the hydrophilic blocks to hydrophobic blocks of the rigid–flexible block molecules at the air–water interface changes continuously as the PEO branches transform from a pancake to a brush conformation and are submerged in the water upon compression. As the surface pressure increases from the onset to 10 mNm^{-1} , the compression ratio of the PEO

branches decreases to 2% and the effective contents of the aromatic rod (W_{aromatic}') increases from 56 wt% to 97 wt%.^[37] This indicates that most of the PEO branches are submerged in the water subphase at a surface pressure of 10 mNm^{-1} and the following steep increase in the surface pressure is mainly caused by crowding the aromatic rod segments. The monolayer is also transferred by different dipping speeds and on the mica substrate, similar fibers were obtained (not shown), suggesting that the dipping speed and the substrate have no effect on the structures formed at the air–water interface.

3. Conclusions

Evaporation-driven ring formation and Langmuir–Blodgett films were obtained by utilizing a novel rigid–flexible block molecule. Our experiments elucidated that the formation of well-shaped rings requires optimal conditions of evaporation rate and solute concentration. Due to the controllable sizes of formed patterns derived from this process, it will be of potential interest

in the design on fluorescence patterns. In the LB films, fine and long, straight fibers were obtained. Combining the analysis of the π -A isotherm data for the molecular areas, the AFM images of the fiber dimensions, water contact angle on the surface hydrophobicity, the UV/Vis and fluorescence data on the benzene ring packing, we concluded that the fibers were formed by π - π stacking interaction of the aromatic rod segments, which transformed from the face-on conformation at the onset of the surface pressure to the edge-on conformation as the PEO branches dissolved into water subphase upon compression. The surface patterning of the rings and fibers involving an optical fluorescent rigid–flexible block molecules described herein can easily be controlled, which should be useful in fabricating micro/nanoscale devices based on polymer matrix.

Acknowledgements

This work was supported by the National Creative Research Initiative Program. The BK21 program of the Ministry of Education and Human Resources Development are gratefully acknowledged. The authors thank Liyu Lin in the Department of Mechanical Engineering, Yonsei University for assistance with water contact angle measurements.

Keywords: block copolymers · droplet evaporation · Langmuir–Blodgett films · nanostructures · surface chemistry

[1] a) M. Gaal, C. Gadermaier, H. Plank, E. Moderegger, A. Pogantsch, G. Leising, E. J. W. List, *Adv. Mater.* **2003**, *15*, 1165–1167; b) C. Kallinger, M. Hilmer, A. Haugeneder, M. Perner, W. Spirkl, U. Lemmer, J. Feldmann, U.

- Scherf, K. Mullen, A. Gombert, V. Wittwer, *Adv. Mater.* **1998**, *10*, 920–923.
- [2] a) C. Kim, P. E. Burrows, S. R. Forrest, *Science* **2000**, *288*, 831–833; b) Y. Koide, Q. W. Wang, J. Cui, D. D. Benson, T. J. Marks, *J. Am. Chem. Soc.* **2000**, *122*, 11266–11267.
- [3] H. Gau, S. Herminghaus, P. Lenz, R. Lipowsky, *Science* **1999**, *283*, 46–49.
- [4] a) T. A. Taton, G. Lu, C. A. Mirkin, *J. Am. Chem. Soc.* **2001**, *123*, 5164–5165; b) J. H. Fendler, *Chem. Mater.* **2001**, *13*, 3196–3210.
- [5] H. Xu, R. Hong, T. X. Lu, O. Uzun, V. M. Rotello, *J. Am. Chem. Soc.* **2006**, *128*, 3162–3163.
- [6] M. H. V. Werts, M. Lambert, J. P. Bourgoign, M. Brust, *Nano Lett.* **2002**, *2*, 43–47.
- [7] Q. J. Guo, X. W. Teng, S. Rahman, H. Yang, *J. Am. Chem. Soc.* **2003**, *125*, 630–631.
- [8] a) P. J. Thomas, G. U. Kulkarni, C. N. R. Rao, *J. Mater. Chem.* **2004**, *14*, 625–628; b) S. T. Liu, R. Maoz, J. Sagiv, *Nano Lett.* **2004**, *4*, 845–851.
- [9] P. Maury, M. Escalante, D. N. Reinhoudt, J. Huskens, *Adv. Mater.* **2005**, *17*, 2718–2723.
- [10] M. Geissler, Y. N. Xia, *Adv. Mater.* **2004**, *16*, 1249–1269.
- [11] a) R. D. Deegan, O. Bakajin, T. F. Dupont, G. Huber, S. R. Nagel, T. A. Witten, *Nature* **1997**, *389*, 827–829; b) R. D. Deegan, *Phys. Rev. E* **2000**, *61*, 475–485; c) R. D. Deegan, O. Bakajin, T. F. Dupont, G. Huber, S. R. Nagel, T. A. Witten, *Phys. Rev. E* **2000**, *62*, 756–765; d) E. Rabani, D. R. Reichman, P. L. Geissler, L. E. Brus, *Nature* **2003**, *426*, 271–274.
- [12] a) T. Okubo, S. Kanayama, H. Ogawa, M. Hibino, K. Kimura, *Colloid Polym. Sci.* **2004**, *282*, 230–235; b) T. Okubo, H. Kimura, T. Kawai, H. Niimi, *Langmuir* **2003**, *19*, 6014–6018; c) T. Okubo, A. Tsuchida, T. Okuda, K. Fujitsuna, M. Ishikawa, T. Morita, T. Tada, *Colloids Surf. A* **1999**, *153*, 515–524.
- [13] a) M. Shimomura, T. Sawadaishi, *Curr. Opin. Colloid Interface Sci.* **2001**, *6*, 11–16; b) O. Karthaus, N. Maruyama, X. Cieren, M. Shimomura, H. Hasegawa, T. Hashimoto, *Langmuir* **2000**, *16*, 6071–6076.
- [14] a) P. C. Ohara, J. R. Heath, W. M. Gelbart, *Angew. Chem.* **1997**, *109*, 1120–1122; *Angew. Chem. Int. Ed. Engl.* **1997**, *36*, 1078–1080; b) P. C. Ohara, W. M. Gelbart, *Langmuir* **1998**, *14*, 3418–3424; c) T. Vossmeier, S.-W. Chung, W. M. Gelbart, J. R. Heath, *Adv. Mater.* **1998**, *10*, 351–353.
- [15] a) C. J. Brinker, A. Sellinger, P. M. Weiss, A. Nguyen, Y. Lu, R. A. Assink, W. Gong, *Nature* **1998**, *394*, 256–260; b) C. J. Brinker, Y. Lu, A. Sellinger, H. Fan, *Adv. Mater.* **1999**, *11*, 579–585; c) Y. Lu, H. Fan, N. Doke, D. A. Loy, R. A. Assink, D. A. LaVan, C. J. Brinker, *J. Am. Chem. Soc.* **2000**, *122*, 5258–5261.
- [16] a) A. P. Sommer, R.-P. Franke, *Nano Lett.* **2003**, *3*, 573–575; b) A. P. Sommer, M. Ben-Moshe, S. Magdassi, *J. Phys. Chem. B* **2004**, *108*, 8–10.
- [17] A. P. Sommer, N. Rozlosnik, *Cryst. Growth Des.* **2005**, *5*, 551–557.
- [18] a) B.-J. de Gans, P. C. Duineveld, U. S. Schubert, *Adv. Mater.* **2004**, *16*, 203–213; b) B.-J. de Gans, U. S. Schubert, *Langmuir* **2004**, *20*, 7789–7793; c) S. Magdassi, M. Ben-Moshe, *Langmuir* **2003**, *19*, 939–942.
- [19] a) A. Ulman, *An Introduction to Ultrathin Organic Films: From Langmuir-Blodgett to Self-Assembly*, Academic Press, Boston, **1991**; b) P. Moraille, A. Badia, *Langmuir* **2002**, *18*, 4414–4419; c) P. Moraille, A. Badia, *Langmuir* **2003**, *19*, 8041–8049.
- [20] a) M. Gleiche, L. F. Chi, H. Fuchs, *Nature* **2000**, *403*, 173–175; b) X. D. Chen, S. Lenhart, M. Hirtz, N. Lu, H. Fuchs, L. F. Chi, *Acc. Chem. Res.* **2007**, *40*, 393–401; c) X. D. Chen, M. Hirtz, A. L. Rogach, D. V. Talapin, H. Fuchs, L. F. Chi, *Nano Lett.* **2007**, *7*, 3483–3488; d) L. F. Chi, S. Jacobi, B. Anczykowski, M. Overs, H.-J. Schäfer, H. Fuchs, *Adv. Mater.* **2000**, *12*, 25–30; e) L. Zhang, N. Gaponik, J. Müller, U. Plate, H. Weller, G. Erker, H. Fuchs, A. L. Rogach, L. F. Chi, *Small* **2005**, *1*, 524–527.
- [21] a) M. Lee, B.-K. Cho, W.-C. Zin, *Chem. Rev.* **2001**, *101*, 3869–3892; b) J.-K. Kim, E. Lee, Z. Huang, M. Lee, *J. Am. Chem. Soc.* **2006**, *128*, 14022–14023; c) W.-Y. Yang, E. Lee, M. Lee, *J. Am. Chem. Soc.* **2006**, *128*, 3484–3485.
- [22] E. Lee, J.-K. Kim, M. Lee, *Angew. Chem.* **2009**, *121*, 3711–3714; *Angew. Chem. Int. Ed.* **2009**, *48*, 3657–3660.
- [23] S. Szunerits, R. Boukherroub, *Langmuir* **2006**, *22*, 1660–1663.
- [24] a) K. Larson, D. Vaknin, O. Villavicencio, D. McGrath, V. V. Tsukruk, *J. Phys. Chem. B* **2002**, *106*, 7246–7251; b) L. Liu, K.-S. Moon, R. Gunawidjaja, E. Lee, V. V. Tsukruk, M. Lee, *Langmuir* **2008**, *24*, 3930–3936; c) L. Liu, J.-K. Kim, M. Lee, *ChemPhysChem* **2008**, *9*, 1585–1592.
- [25] S. N. Magonov, V. Elings, M.-H. Whangbo, *Surf. Sci.* **1997**, *375*, L385–391.
- [26] a) M. Maillard, L. Motte, A. T. Ngo, M. P. Pileni, *J. Phys. Chem. B* **2000**, *104*, 11871–11877; b) C. Stowell, B. A. Korgel, *Nano Lett.* **2001**, *1*, 595–600.
- [27] a) A. M. Gonçalves da Silva, E. J. M. Filipe, J. M. R. d'Oliveira, J. M. G. Martinho, *Langmuir* **1996**, *12*, 6547–6553; b) A. M. Gonçalves da Silva, A. L. Simões Gamboa, J. M. G. Martinho, *Langmuir* **1998**, *14*, 5327–5330.
- [28] a) H. D. Bijsterbosch, V. O. de Haan, A. W. de Graaf, M. Mellma, F. A. M. Leemakers, M. A. Cohen Stuart, A. A. van Well, *Langmuir* **1995**, *11*, 4467–4473; b) J. K. Cox, K. Yu, B. Constantine, A. Eisenberg, R. B. Lennox, *Langmuir* **1999**, *15*, 7714–7718.
- [29] The area of PEO monomeric units oriented at the water surface and hydrogen-bonded with one to three water molecules is 0.22–0.28 nm² (J. K. Cox, K. Yu, A. Eisenberg, R. B. Lennox, *Phys. Chem. Chem. Phys.* **1999**, *1*, 4417–4421; M. C. Fauré, P. Bassereau, M. A. Carignano, I. Szleifer, Y. Gallot, D. Andelman, *Eur. Phys. J. B* **1998**, *3*, 365–375). The area occupied by the aromatic rod segment in face-on conformation can be calculated by the CPK model. So the area occupied by a molecule can be obtained by the area of the aromatic rod segment plus the area of the PEO branches.
- [30] X. Ji, C. Wang, J. Xu, J. Zheng, K. M. Gattas-Asfura, R. M. Leblanc, *Langmuir* **2005**, *21*, 5377–5382.
- [31] a) K. L. Genson, D. Vaknin, O. Villavicencio, D. V. McGrath, V. V. Tsukruk, *J. Phys. Chem. B* **2002**, *106*, 11277–11284; b) H. Riegler, K. Spratte, *Thin Solid Films* **1992**, *210*, 9–12.
- [32] a) S. Peleshanko, R. Gunawidjaja, S. Petrash, V. V. Tsukruk, *Macromolecules* **2006**, *39*, 4756–4766; b) S. Peleshanko, K. D. Anderson, M. Goodman, M. D. Determan, S. K. Mallapragada, V. V. Tsukruk, *Langmuir* **2007**, *23*, 25–30.
- [33] S. Schwiegk, T. Xu, Y. Vahlenkamp, G. Wegner, *Macromolecules* **1992**, *25*, 2513–2525.
- [34] T. Miteva, L. Palmer, L. Kloppenburg, D. Neher, U. H. F. Bunz, *Macromolecules* **2000**, *33*, 652–654.
- [35] L. Chen, C. Gristina, J. Perlstein, D. G. Whitten, *J. Phys. Chem. B* **1999**, *103*, 9161–9167.
- [36] a) J. Kim, T. M. Swager, *Nature* **2001**, *411*, 1030–1034; b) J. Kim, I. A. Levitsky, D. T. McQuade, T. M. Swager, *J. Am. Chem. Soc.* **2002**, *124*, 7710–7718.
- [37] The area of the aromatic rod (A_{aromatic}) approximates the limiting area of the molecule and keeps constant during compression. Therefore, the area of PEO at a certain pressure ($A_{\text{PEO},\pi}$) can be calculated according to the pressure–area isotherm. The compression ratio of PEO chains is considered as the ratio of $A_{\text{PEO},\pi}$ to the area at the onset of pressure elevation ($A_{\text{PEO},0}$). Finally, the effective contents of aromatic rod ($W_{\text{aromatic}}^{\text{eff}}$) could be estimated as $W_{\text{aromatic}}^{\text{eff}} = 1/(A_{\text{PEO},\pi}/A_{\text{PEO},0} \times W_{\text{PEO}}\%/W_{\text{aromatic}}\% + 1)$.

Received: October 14, 2009

Published online on December 28, 2009